









RESEARCH ARTICLE | MAY 30 2024

# Near-field probes for sensitive detectorless near-field nanoscopy in the 2.0–4.6 THz range

Valentino Pistore ; Chiara Schiattarella ; Leonardo Viti ; Thomas Siday ; Michael B. Johnston ; Oleg Mitrofanov ; Miriam S. Vitiello  

 Check for updates

*Appl. Phys. Lett.* 124, 221105 (2024)

<https://doi.org/10.1063/5.0179714>



View  
Online



Export  
Citation

03 July 2024 07:24:18



## Journal of Applied Physics

Special Topic:

Disordered Materials at the Atomic Scale

Guest Editors: Jaeyun Moon, Matteo Baggioli

[Submit Today!](#)

# Near-field probes for sensitive detectorless near-field nanoscopy in the 2.0–4.6 THz range

Cite as: Appl. Phys. Lett. **124**, 221105 (2024); doi: [10.1063/5.0179714](https://doi.org/10.1063/5.0179714)

Submitted: 4 October 2023 · Accepted: 18 May 2024 ·

Published Online: 30 May 2024



View Online



Export Citation



CrossMark

Valentino Pistore,<sup>1</sup> Chiara Schiattarella,<sup>1</sup> Leonardo Viti,<sup>1</sup> Thomas Siday,<sup>2</sup> Michael B. Johnston,<sup>2</sup> Oleg Mitrofanov,<sup>3</sup> and Miriam S. Vitiello<sup>1,a)</sup>

## AFFILIATIONS

<sup>1</sup>NEST, CNR-NANO and Scuola Normale Superiore, 56127 Pisa, Italy

<sup>2</sup>Department of Physics, University of Oxford, Oxford OX1 3PU, United Kingdom

<sup>3</sup>University College London, Electronic and Electrical Engineering, London WC1E 7JE, United Kingdom

<sup>a)</sup> Author to whom correspondence should be addressed: [miriam.vitiello@sns.it](mailto:miriam.vitiello@sns.it)

## ABSTRACT

Imaging and spectroscopy at terahertz (THz) frequencies have become key methods for fundamental studies across the physical sciences. With the emergence of nanoscale materials and devices, holding great promise for photonics, electronics, and communication technologies, the search for THz analysis at the nanoscale arises. Detectorless THz near-field nanoscopy emerged as a versatile method for hyperspectral mapping of light–matter interaction phenomena in bi-dimensional materials and systems. However, it is strongly limited by the weak scattering efficiencies of atomic force microscope (AFM) tips. Here, we experimentally evaluate the performance of unconventional AFM tip shapes to enhance the scattering efficiency, at three frequencies, namely, 2.0, 3.0, and 4.6 THz. The impact of tip geometry is corroborated by numerical simulations. The shorter shank length of the evaluated tips provides a very compelling alternative to commercial tips at frequencies  $>2$  THz.

© 2024 Author(s). All article content, except where otherwise noted, is licensed under a Creative Commons Attribution (CC BY) license (<https://creativecommons.org/licenses/by/4.0/>). <https://doi.org/10.1063/5.0179714>

In optical microscopy, overcoming the diffraction limit is the primary condition for accessing the physical information contained in volumes smaller than the radiation wavelength. This is especially critical in the terahertz (THz) frequency range, where the wavelength range (30–300  $\mu\text{m}$ ) would otherwise restrict observation to macroscopic samples.

In the last two decades, scattering-type scanning near-field optical microscopy (s-SNOM) has emerged as one of the primary tools to achieve sub-micrometric spatial resolution at long wavelengths (66–300  $\mu\text{m}$ ),<sup>1–3</sup> with applications to nanoscale imaging of material and device properties.<sup>2,4,5</sup> THz s-SNOM has been implemented with several THz sources, providing impressive performances in terms of frequency coverage ( $>5$  THz)<sup>6</sup> and spatial resolution ( $<15$  nm).<sup>7</sup>

A limiting factor toward the widespread adoption of this technique is the scarcity of fast and sensitive THz detectors, with hot-electron bolometers,<sup>6</sup> field-effect transistors,<sup>8</sup> and Schottky diodes<sup>7</sup> being typical choices. An alternative can be found in the self-mixing (SFMX) effect of THz quantum cascade lasers (QCLs).<sup>5,9,10</sup> This allows to retrieve the near-field information, enabling the use of QCLs as both sources and detectors for s-SNOM experimental setups.

THz QCLs are employed in combination with s-SNOM systems because of their compactness (typical volume  $<0.01$  mm<sup>3</sup>), high power output up to hundreds of mW in continuous-wave (CW) operation,<sup>11</sup> frequency tunability,<sup>12</sup> and spectral coverage from 1.3 to 5.4 THz.<sup>13</sup> Very recently, hyperspectral imaging and spectroscopy have been demonstrated by exploiting frequency comb emission in QCLs, which opens intriguing perspective applications in the field of THz nanoscopy.<sup>14</sup>

At the core of the s-SNOM system is the microscope's metallic probe, which localizes and enhances the radiation at its apex, enabling to probe the nanometric volume of material beneath with the evanescent field of the coupled electromagnetic wave. The nontrivial scattering process occurring at the tip brings the near-field information to the detection unit.<sup>15</sup> It is therefore of utmost importance to understand the role played by geometric and material parameters of the probe in determining the coupling, localization, and scattering of electromagnetic radiation. This has stimulated the experimental and numerical investigation of different probes to improve the spatial resolution and the signal to noise ratio (SNR) of the optical signal.<sup>16–20</sup> In these previous works, the typical probe structure is embodied by a truncated cone

with a hemispherical apex.<sup>17,18</sup> This representation has revealed the role played by the apex radius, tip length, and material on the response of the probe to the incoming radiation. Additional structural elements, such as the cantilever, are usually not implemented in simulations, and their contribution to the near-field response is assumed to be negligible. However, this macroscopic geometry can significantly impact the scattering efficiency and the s-SNOM signal amplitude.

Here, we expand previous studies on THz s-SNOM probes to structures with unconventional shapes, including elephant-trunk and pyramid shaped tips. We perform s-SNOM experiments in a QCL-based detectorless configuration,<sup>2</sup> employing probes with apex radii spanning from 10 to 500 nm and at three distinctive frequencies, namely, 2.0, 3.0, and 4.6 THz. Our experimental results are corroborated by numerical simulations, which allow us to directly evaluate the impact of the tip geometrical parameters onto its performance for s-SNOM systems, highlighting the effect of structural and geometrical elements for each probe.

We performed our near-field measurements employing tips of various shapes and dimensions (see Table I). The geometrical characteristics of each probe are plotted in Figs. 1(a) and 1(b) according to the nominal values provided by the respective producers. Figure 1(b) reports the tips characteristics in terms of shank length and nominal apex radius. The combinations of cantilever length and width as well as the shank length and tip apex comprise a broad range of probe configurations. Scanning electron microscope (SEM) images for each probe are displayed in Figs. 1(c) and 1(f). They highlight the geometrical shapes analyzed in the present work.

The main elements of our experimental setup are a near-SNOM system (Neaspec-Attocube) and a set of single frequency, cryogenically cooled, THz QCLs, each operating as both source and detector. The system is schematically represented in Fig. 2(a). A comprehensive description of the measurement setup is provided in the supplementary material. Throughout all measurements, a constant tapping amplitude of 200 nm is maintained for all tips.

The spatial resolution from the optical signal is better characterized in a flat geometry by scanning across an interface between two media with different dielectric characteristics.<sup>21</sup> This allows, in principle, to avoid “edge-darkening”<sup>22</sup> and other artifacts arising from the interaction of the tip apex and shank with the step edge.<sup>16</sup> A planarization step is neither, however, typically feasible nor desirable for complex structures, as it easily compromises the device performance. Therefore, we evaluated the optical spatial resolution of each probe in the case of a 40 nm-thick Au step on a SiO<sub>2</sub> substrate. Both materials

are standard choices for basic fabrication processes and allow for a straightforward replication of the presented results.

A prototypical amplitude map of the SiO<sub>2</sub>/Au step, measured with the elephant-trunk tip at 2 THz, is displayed in Fig. 2(b). By changing the phase at the beginning of each position along the y-axis, an interference pattern is created, whose Fourier transform enables to retrieve the sample response at the different spectral components of the SFMX signal.

Details on the adopted experimental technique are provided in the supplementary material. In the SFMX based detectorless s-SNOM configuration adopted in the present work, we introduce the optical delay by changing the optical path length between the THz QCL source and the microscope AFM probe. In this arrangement, the SFMX response can show a non-linear dependence on the feedback strength and the operational current of the pumping QCL. This results in the generation of harmonics of the fundamental emission frequency, which do not scale linearly with the scattered field, as visible in Fig. 2(c) and must not be considered in the analysis. The spectral amplitude of the map measured in Fig. 2(b) is reported in Fig. 2(c) from 0 to 7 THz. The harmonics at 4 and 6 THz can be separated from the component at 2 THz, thanks to our approach. From each map, we extracted the line profile perpendicular to the materials interface and performed the fitting of its derivative accounting for the asymmetry of the curve across the interface.<sup>21</sup> More information about the fitting procedure is available in the supplementary material.

The measured topographic and optical resolution at 2 THz for all tips is reported in Fig. 2(d). Let us first consider the measured topographic resolution. For apex radii smaller or comparable to the height of the topographic step (40 nm), tips#1–3 display topographic resolutions exceeding their apex size. This can be primarily attributed to the probe shank contacting the step edge before the tip apex does, introducing an offset to the topographical resolution. For apex radii far exceeding the step height and greater than the tapping amplitude (tips#5–6), the resolution is approximately half of the nominal apex radius due to the “virtual tip sharpening effect.”<sup>7</sup> The optical resolution, on the other hand, scales weakly with the apex radius of the tips. Tip#1 shows ~80 nm resolution, whereas tips#2–4 are all within the 90–105 nm range. These values are within expectations, since there is a consensus in the community that typical THz s-SNOM optical resolutions are in the 50–100 nm range.<sup>23</sup> For very large tip radii, the optical resolution seems to saturate at ~175 nm, which can be explained by the virtual tip sharpening effect.<sup>7</sup> The optical resolution is known to be independent from the radiation wavelength.<sup>23</sup> We confirmed the validity of this observation for tips#3–4 by retrieving the optical resolution

**TABLE I.** Summary of the investigated probes: a numbering for internal reference is given in the first column. The following columns report the code name, manufacturer, nominal apex radius, coating material, and experimentally determined tapping frequency. RMN = Rocky Mountain Nanotechnology; NT = NextTip.

#	Code name	Manufacturer	Tip nominal radius (nm)	Coating	Tapping frequency (kHz)
1	25PtIr300B-10	RMN	10	PtIr	28.39
2	25PtIr200B-40H	RMN	40	PtIr	64.57
3	NT-IR-P-75	NT	53	Au nanoparticles	75.14
4	NT-IR-E-85	NT	80	Au nanoparticles	65.61
5	LRCH250-225C3.0	Team Nanotech	250	Al-reflex	67.22
6	LRCH500-225C3.0	Team Nanotech	500	Al-reflex	71.92

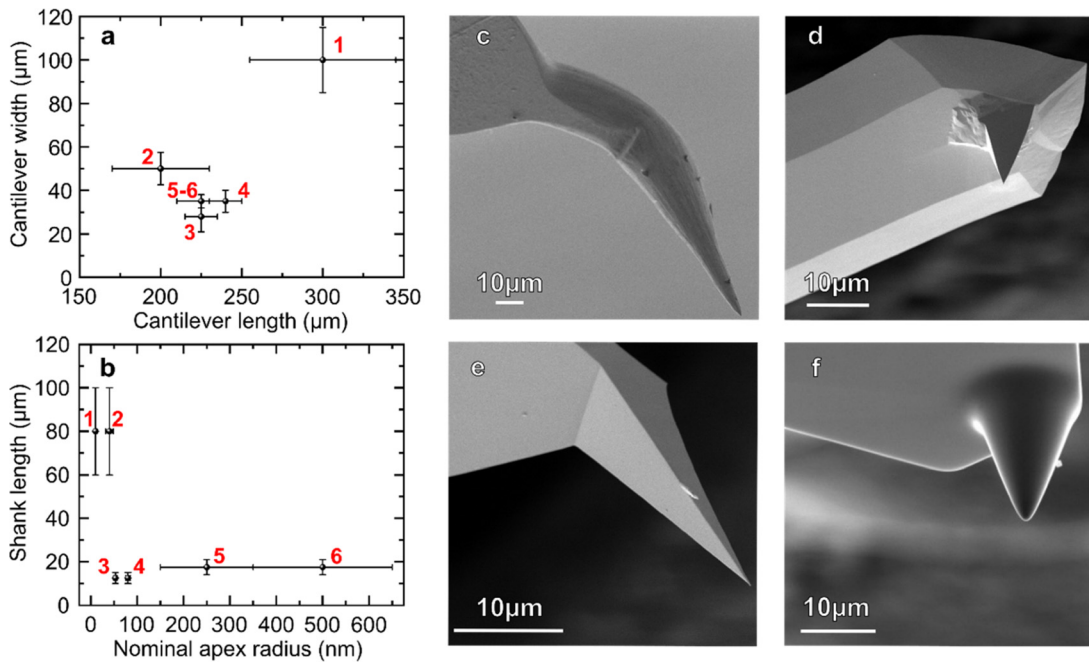


FIG. 1. (a) Nominal cantilever geometrical dimensions for each investigated probe. (b) Nominal shank length and apex radius. The red numbers in (a) and (b) refer to probe numbering of Table I. (c)–(f) SEM images of the investigated probe structures: conical from Rocky Mountain Nanotechnology (RMN) probes (c), pyramidal (d) and elephant-trunk (e) from NextTip (NT), and hemispherical (f) from Team Nanotech.

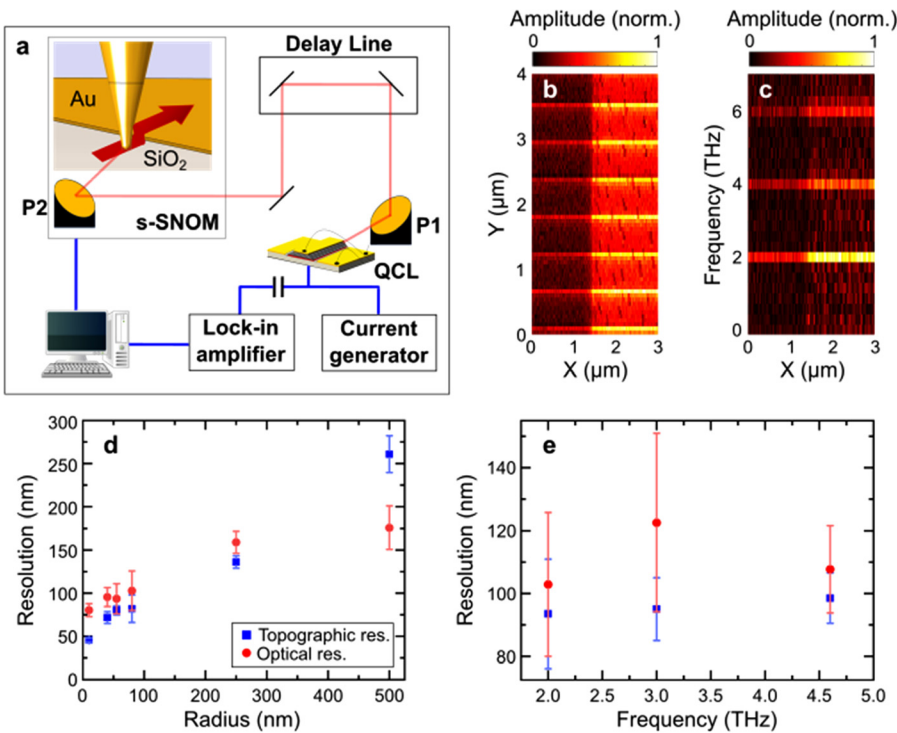


FIG. 2. (a) Schematic of the measurement setup. (b) Amplitude map of the near-field signal demodulated at the second harmonic of the probe tapping frequency on the SiO<sub>2</sub>/Au step. (c) Spectral amplitude map retrieved by Fourier-transforming the complex holographic map of the SiO<sub>2</sub>/Au step, measured at 2 THz. (d) Topographic and optical resolution for all the tips measured at 2 THz. (e) Optical resolution of tip#4 (red dots) and tip#3 (blue square) from 2.0 to 4.6 THz.

03 July 2024 07:24:18

at 3.0 and 4.6 THz. The results are displayed in Fig. 2(e) and show a very marginal increase in the resolution with the radiation frequency.

We then tested the tips by measuring the optical response of a bismuth selenide ( $\text{Bi}_2\text{Se}_3$ ) flake deposited on a  $\text{SiO}_2$  substrate.  $\text{Bi}_2\text{Se}_3$  is a well-known topological insulator<sup>24</sup> with high optical contrast at 2.0 THz. Previous works have already extensively studied the response of  $\text{Bi}_2\text{Se}_3$  flakes at these frequencies,<sup>14,25</sup> which allows to compare our findings with independent experimental campaigns on the same material system.

In order to retrieve the maximum achievable SNR for each tip, we set the delay-line to a position corresponding to a maximum of the amplitude of the SFMX fringes, i.e., we did not separate the spectral

components for this set of measurements. This allows us to compare the raw performance of each tip without the need of elaborate post-processing solutions. The topographic, amplitude, and phase maps of the  $\text{Bi}_2\text{Se}_3$  flake are displayed in Fig. 3.

Each map is acquired with a 25 nm step size, 10 ms integration time per pixel, and the optical signal is demodulated at the second harmonic of the probe tapping frequency. The topographic maps show the presence of a mostly flat  $\sim 95$  nm-thick flake with a much thicker and steeper structure on the bottom-left corner.

One can also observe that the most challenging feature to be resolved is the structure in the bottom-left corner of the flake. Tips#5–

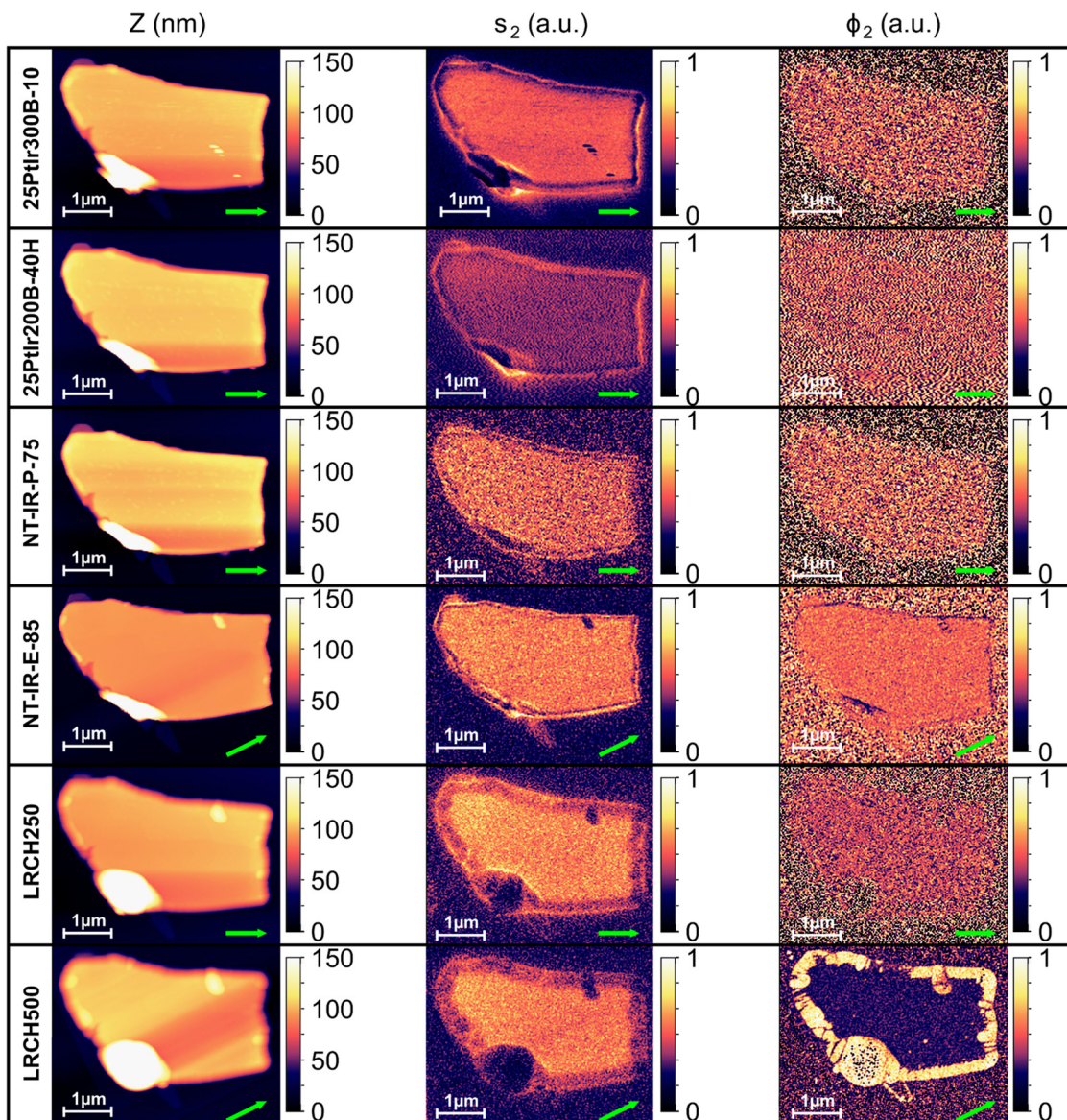


**FIG. 3.** First column: topographical map of the  $\text{Bi}_2\text{Se}_3$  flake imaged with all investigated probes. Second column: optical amplitude map demodulated at the second harmonic of the probe tapping amplitude ( $s_2$ ) of the  $\text{Bi}_2\text{Se}_3$  flake. Third column: optical phase map demodulated at the second harmonic of the probe tapping amplitude ( $\phi_2$ ) of the  $\text{Bi}_2\text{Se}_3$  flake. All maps have been measured at 2 THz.

**TABLE II.** SNR of the amplitude and standard deviation of the phase of the signal retrieved on  $\text{Bi}_2\text{Se}_3$  at 2 THz with each investigated tip.

#	Code name	SNR (amplitude)	Std. dev. phase (rad)
1	25PtIr300B-10	20.5809	0.0393
2	25PtIr200B-40H	6.4324	0.1603
3	NT-IR-P-75	3.6917	0.4377
4	NT-IR-E-85	6.4134	0.1569
5	LRCH250-225C3.0	6.9189	0.1444
6	LRCH500-225C3.0	6.1793	0.1657

6, having a very large radius, are unable to correctly resolve such a high ( $\sim 300$  nm) and narrow feature, imaging an elliptical object, which is the result of the convolution of the flake edge structure in that position with the tip shape. Tips#1–2, having the smaller radius and the smaller spatial resolution [Fig. 2(d)], are expected to provide the most accurate imaging of the feature. Counterintuitively, this is not the case for tip#1, which shows a local response we attribute to the interaction of the probe shank with the feature. In fact, the same tip provides a very clear image of the rest of the flake, supporting our conclusion. Tip#2 provides a more accurate imaging of the corner, with a clear similarity with the images provided by NextTip probes.

The amplitude maps of the  $\text{Bi}_2\text{Se}_3$  flake are used to retrieve the SNR at a fixed optical delay, here defined as the ratio between the average amplitude of the near-field signal and its standard deviation. This is done by evaluating the average value of the  $s_2$  signal and its standard deviation over a  $1\ \mu\text{m} \times 1\ \mu\text{m}$  square at the center of the flake. Since the average phase can take any value between 0 and  $2\pi$ , we report the standard deviation of the phase instead of its SNR. The results are summarized in Table II. Most tips provide an SNR just above 6, with tip#1 reaching a considerable SNR above 20, which we attribute to the non-linear response of the SFMX. Tip#3, on the other hand, shows poor performance at 2.0 THz with an SNR below 4. The standard deviation of the phase maps agrees with the observed SNR trend, with the minimum standard deviation for tip#1 and the maximum for tip#3. We also wish to highlight that tip#4 is the only probe which has provided an optical map where the sharp structure at the lower left corner

is unambiguously shown to be an integral part of the flake edge. It has also revealed the presence of a smaller part of the flake, with lower thickness and contrast, just below the main flake. The same small feature is hinted in the amplitude map of tip#3 and is clearly revealed in the phase map of tip#6. The latter provides a phase map where the contour of all the imaged objects is very different from both the  $\text{SiO}_2$  and the  $\text{Bi}_2\text{Se}_3$  phase. Of course, due to its very large radius, this tip largely overestimates the border extension, but its capability to optically reveal nearly invisible features makes it useful to identify the edges of materials with low contrast. One should expect an increase in signal strength with larger tip apices, as it was demonstrated previously experimentally and numerically.<sup>7</sup>

The sensitivity of s-SNOM probes is in large part a result of their scattering efficiency, which, at THz frequencies, is dominated by the macroscopic geometry of the probe shank and cantilever.<sup>18,26,27</sup> To gain insight into how the macroscopic geometry of the tips affects the scattering efficiency, we model the response of each tip using a commercial finite-difference time-domain solver (Lumerical, Inc.). The experimental SNR is given by three contributions. The first is related to the tip shank length and geometrical shape, the second to the tip apex radius, and the third to the SFMX response of the QCL. By removing the influence of the tip radius from our simulations, we can isolate the contribution of the tip geometry to the SNR.

To isolate the influence of macroscopic tip geometry on scattering efficiency, we maintain a consistent apex radius for all the tips in the numerical model ( $R = 100$  nm), as the apex radius affects both field enhancement and scattering efficiency, and its influence can be understood using analytical scattering models.<sup>28</sup> We also keep the tip-sample distance constant in the simulation, which is justified as the tip tapping amplitude  $A$  is held constant in all experimental tests and is on the scale of 200 nm—orders of magnitude smaller than the THz wavelength. Under these conditions, the field enhancement at the tip apex becomes an analogue for scattering efficiency, which we compute by sampling the magnitude of the electric field  $|E|$  between the apex of the tip and metal sample surface [Fig. 4(a)].

Figure 4(b) shows the calculated field enhancement at the apex for three of the experimentally tested probes: the RMN, the NextTip elephant-trunk, and pyramidal tips. All tips show strong Fabry Perot-like resonances originating from reflections along the cantilever, which

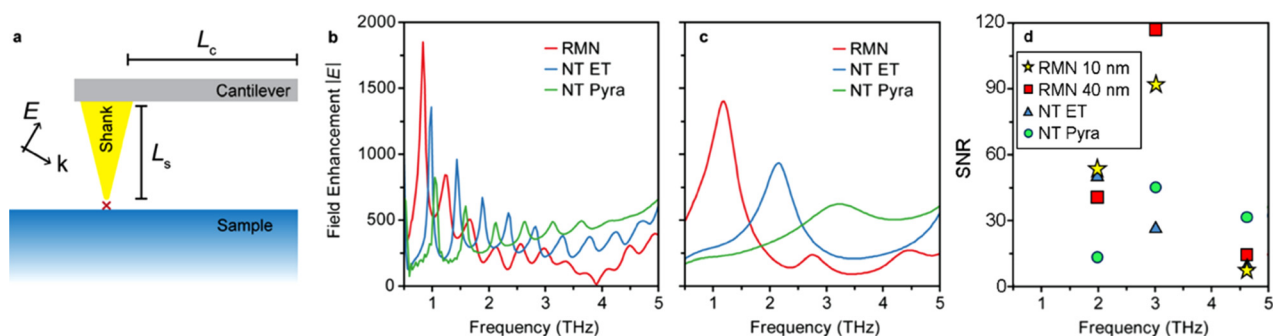


**FIG. 4.** Finite-difference time-domain simulations of the field enhancement at the apex of near-field probes. (a) Schematic of the numerical model. The tip, with shank length  $L_s$  and cantilever length  $L_c$ , is positioned above a metal surface and excited with a Gaussian beam at an incidence angle of  $60^\circ$ . The field enhancement is sampled using a monitor positioned just below the tip apex (red cross). (b) Magnitude field enhancement  $|E|$  at the apex of the RMN probe, NextTip elephant-trunk (NT ET) and Pyramidal (NT Pyra) tips. (c) Field enhancement at the probe apex when the cantilever is removed, highlighting the influence of the tip shank. (d) Experimental signal to noise ratio (SNR) for the RMN probes (tip#1–2) and NT probes (tip#3–4) at 2.0, 3.0, and 4.6 THz, as obtained from the line profiles from holographic measurements on the Au sample.

has been observed previously both in time resolved measurements of near-field scattering with RMN tips and in numerical models.<sup>27</sup> We note that these reflections are typically weaker in the experiment as reflections at the end of the cantilever are damped by the substrate—the large size of this component is impractical to model numerically. Yet, even here some distinctive differences emerge. Below  $\sim 2.0$  THz, the enhancement at the RMN tip apex is strongest. However, as the frequency increases, the field enhancement at the apex of both NextTip probes begins to surpass that of the RMN tip.

The differences shown in Fig. 4(b) must be emerging from the variation in shank geometry because the cantilever length is kept constant ( $L_c = 225 \mu\text{m}$ ) in the simulations. To isolate the impact of the shank further, we simulate the tips with the cantilever removed [Fig. 4(c)]. Here, clear peaks emerge in the field enhancement spectra and occur at different frequencies for each tip. The reason for this increase becomes immediately clear on inspection of the shaft lengths extracted from SEM images:  $L_s = 80, 25, \text{ and } 16 \mu\text{m}$  for the RMN, elephant-trunk, and pyramidal tip, respectively. This is precisely the response expected for a resonant dipole antenna, where the resonant frequency is inversely proportional to the antenna length.<sup>18,26</sup> Hence, the shorter shank length of the elephant-trunk and pyramidal tips provides a compelling alternative to RMN tips when the measurement frequency extends above 2.0 THz.

The simulation results allow us to estimate the expected signal strength from each tip structure in a broad frequency range up to 5 THz. We note that the simulations do not account for the difference in the probe apex radii. Therefore, in addition to the enhancement due to tip shape, one should expect an increase in signal strength with larger tip apices, as it was demonstrated previously experimentally and numerically.<sup>7</sup>

Experimentally, the better estimate for the signal strength is given by the amplitude SNR [Fig. 4(d)], which shows the SNR for the RMN probes (tip#1–2) and NT probes (tip#3–4) at 2.0, 3.0 and 4.6 THz as obtained from the line profiles from holographic measurements on the Au sample. It must be noticed that the influence of each individual QCL response makes the comparison between the SNR at different frequencies unreliable, while it can be still carried out at the single frequencies. Just below 2 THz, simulations [Figs. 4(b) and 4(c)] predict the RMN probes and the elephant-trunk probe to display similarly strong field enhancement. Indeed, this is observed experimentally even for tip#1, hence confirming that the high SNR value in Table II is the result of a non-linear SFMX response, which our holographic approach can effectively address. In the experiments, both RMN probes display a significant increase in the SNR around 3.0 THz, which may be indicative of a smaller shank length compared to the  $80 \mu\text{m}$  reported by the producer. In fact, RMN probes suffer the most from shank length uncertainty [Fig. 1(b)]. Tip#4 performs better in the experiments than tip#3 at 3 THz and better than all other probes at 4.6 THz, which correlates nicely with our simulations.

Finally, tip#5–6 exhibit performance in line with small radii tips (see Table II) at 2.0 THz, aside from the inevitable degradation of the image sharpness although mitigated by the virtual tip sharpening effect. The effect of highlighted material borders even in the absence of a good contrast is a positively unexpected feature displayed by tip#6, whose investigation is, however, beyond the scope of the present work.

See the supplementary material for measurement set up, near-field maps, and fitting procedure for resolution retrieval.

We acknowledge Belen Sanz, Miriam Moreno, and Jose Maria Garcia from the company NextTip for fabricating and providing the NT-IR-P-75 and NT-IR-E-85 AFM tips. This work was supported by the European Research Council through the ERC Proof of Concept Grant STAR (101081567) and EPSRC Grant EP/T025077/1.

## AUTHOR DECLARATIONS

### Conflict of Interest

The authors have no conflicts to disclose.

### Author Contributions

**Valentino Pistore:** Data curation (equal); Formal analysis (equal); Investigation (equal); Methodology (equal); Writing – review & editing (lead). **Chiara Schiattarella:** Investigation (supporting). **Leonardo Viti:** Data curation (equal); Investigation (equal); Methodology (equal); Writing – review & editing (equal). **Thomas Siday:** Investigation (supporting). **Michael B. Johnston:** Resources (supporting). **Oleg Mitrofanov:** Investigation (supporting). **Miriam S. Vitiello:** Conceptualization (lead); Resources (lead); Supervision (lead); Writing – review & editing (equal).

### DATA AVAILABILITY

The data that support the findings of this study are available from the corresponding author upon reasonable request.

### REFERENCES

- A. J. Huber, F. Keilmann, J. Wittborn, J. Aizpurua, and R. Hillenbrand, “Terahertz near-field nanoscopy of mobile carriers in single semiconductor nanodevices,” *Nano Lett.* **8**, 3766–3770 (2008).
- M. C. Giordano, S. Mastel, C. Liewald, L. L. Columbo, M. Brambilla, L. Viti, A. Politano, K. Zhang, L. Li, A. G. Davies, E. H. Linfield, R. Hillenbrand, F. Keilmann, G. Scamarcio, and M. S. Vitiello, “Phase-resolved terahertz self-detection near-field microscopy,” *Opt. Express* **26**, 18423–18435 (2018).
- C. Liewald, S. Mastel, J. Hesler, A. J. Huber, R. Hillenbrand, and F. Keilmann, “All-electronic terahertz nanoscopy,” *Optica* **5**, 159–163 (2018).
- A. J. L. Adam, “Review of near-field terahertz measurement methods and their applications,” *J. Infrared Millim. Terahertz Waves* **32**, 976–1019 (2011).
- R. Degl’Innocenti, R. Wallis, B. Wei, L. Xiao, S. J. Kindness, O. Mitrofanov, P. Braeuninger-Weimer, S. Hofmann, H. E. Beere, and D. A. Ritchie, “Terahertz nanoscopy of plasmonic resonances with a quantum cascade laser,” *ACS Photonics* **4**, 2150–2157 (2017).
- F. Kuschewski, H.-G. von Ribbeck, J. Döring, S. Winnerl, L. M. Eng, and S. C. Kehr, “Narrow-band near-field nanoscopy in the spectral range from 1.3 to 8.5 THz,” *Appl. Phys. Lett.* **108**, 113102 (2016).
- C. Maissen, S. Chen, E. Nikulina, A. Govyadinov, and R. Hillenbrand, “Probes for ultrasensitive THz nanoscopy,” *ACS Photonics* **6**, 1279–1288 (2019).
- M. M. Wiecha, R. Kapoor, A. V. Chernyadiev, K. Ikamas, A. Lisauskas, and H. G. Roskos, “Antenna-coupled field-effect transistors as detectors for terahertz near-field microscopy,” *Nanoscale Adv.* **3**, 1717–1724 (2021).
- P. Dean, Y. L. Lim, A. Valavanis, R. Kliese, M. Nikolić, S. P. Khanna, M. Lachab, D. Indjin, Z. Ikonić, P. Harrison, A. D. Rakić, E. H. Linfield, and A. G. Davies, “Terahertz imaging through self-mixing in a quantum cascade laser,” *Opt. Lett.* **36**, 2587–2589 (2011).
- K. S. Reichel, E. A. A. Pogna, S. Biasco, L. Viti, A. D. Gaspare, H. E. Beere, D. A. Ritchie, and M. S. Vitiello, “Self-mixing interferometry and near-field nanoscopy in quantum cascade random lasers at terahertz frequencies,” *Nanophotonics* **10**, 1495–1503 (2021).

- <sup>11</sup>L. Weijiang, Y. Li, Y. Ma, Y. Xu, J. Liu, N. Zhuo, Q. Lu, L. Wang, J. Zhang, S. Zhai, S. Liu, and F. Liu, "Continuous-wave terahertz quantum cascade laser based on a hybrid bound to bound quantum design," *Front. Photonics* **3**, 1–6 (2022).
- <sup>12</sup>C. Sirtori, S. Barbieri, and R. Colombelli, "Wave engineering with THz quantum cascade lasers," *Nat. Photonics* **7**, 691–701 (2013).
- <sup>13</sup>B. Wen and D. Ban, "High-temperature terahertz quantum cascade lasers," *Prog. Quantum Electron.* **80**, 100363 (2021).
- <sup>14</sup>V. Pistore, E. A. A. Pogna, L. Viti, L. Li, G. A. Davies, E. H. Linfield, and M. S. Vitiello, "Self-induced phase locking of terahertz frequency combs in a phase-sensitive hyperspectral near-field nanoscope," *Adv. Sci.* **9**, 2200410 (2022).
- <sup>15</sup>F. Keilmann and R. Hillenbrand, "Near-field microscopy by elastic light scattering from a tip," *Philos. Trans. R. Soc. Lond. Ser. Math. Phys. Eng. Sci.* **362**(1817), 787–805 (2004).
- <sup>16</sup>V. E. Babicheva, S. Gamage, M. I. Stockman, and Y. Abate, "Near-field edge fringes at sharp material boundaries," *Opt. Express* **25**(20), 23935–23944 (2017).
- <sup>17</sup>F. Mooshammer, M. A. Huber, F. Sandner, M. Plankl, M. Zizlsperger, and R. Huber, "Quantifying nanoscale electromagnetic fields in near-field microscopy by Fourier demodulation analysis," *ACS Photonics* **7**(2), 344–351 (2020).
- <sup>18</sup>T. Siday, L. L. Hale, R. I. Hermans, and O. Mitrofanov, "Resonance-enhanced terahertz nanoscopy probes," *ACS Photonics* **7**(3), 596–601 (2020).
- <sup>19</sup>G. Conrad, C. B. Casper, E. T. Ritchie, and J. M. Atkin, "Quantitative modeling of near-field interactions incorporating polaritonic and electrostatic effects," *Opt. Express* **30**(7), 11619–11632 (2022).
- <sup>20</sup>C. Silvestri, L. L. Columbo, and M. Brambilla, "Retrieval of the dielectric properties of a resonant material in the terahertz region via self-detection near field optical microscopy," *IEEE J. Sel. Top. Quantum Electron.* **29**(5), 1–11 (2023).
- <sup>21</sup>S. Mastel, A. A. Govyadinov, C. Maissen, A. Chuvilin, A. Berger, and R. Hillenbrand, "Understanding the image contrast of material boundaries in IR nanoscopy reaching 5 nm spatial resolution," *ACS Photonics* **5**(8), 3372–3378 (2018).
- <sup>22</sup>X. Chen, Z. Yao, S. G. Stanciu, D. N. Basov, R. Hillenbrand, and M. Liu, "Rapid simulations of hyperspectral near-field images of three-dimensional heterogeneous surfaces," *Opt. Express* **29**(24), 39648–39668 (2021).
- <sup>23</sup>M. M. Wiecha, A. Soltani, and H. G. Roskos, *Terahertz Nano-Imaging with s-SNOM* (IntechOpen, 2021). DOI:10.5772/intechopen.99102.
- <sup>24</sup>H. Zhang, C.-X. Liu, X.-L. Qi, X. Dai, Z. Fang, and S.-C. Zhang, "Topological insulators in Bi<sub>2</sub>Se<sub>3</sub>, Bi<sub>2</sub>Te<sub>3</sub> and Sb<sub>2</sub>Te<sub>3</sub> with a single Dirac cone on the surface," *Nat. Phys.* **5**(6), 438–442 (2009).
- <sup>25</sup>E. A. A. Pogna, L. Viti, A. Politano, M. Brambilla, G. Scamarcio, and M. S. Vitiello, "Mapping propagation of collective modes in Bi<sub>2</sub>Se<sub>3</sub> and Bi<sub>2</sub>Te<sub>2.2</sub>Se<sub>0.8</sub> topological insulators by near-field terahertz nanoscopy," *Nat. Commun.* **12**(1), 6672 (2021).
- <sup>26</sup>S. Mastel, M. B. Lundberg, P. Alonso-Gonzalez *et al.*, "Terahertz nanofocusing with cantilevered terahertz-resonant antenna tips," *Nano Lett.* **17**(11), 6526 (2017).
- <sup>27</sup>M. Plankl, P. E. Faria Junior, F. Mooshammer *et al.*, "Subcycle contact-free nanoscopy of ultrafast interlayer transport in atomically thin heterostructures," *Nat. Photonics* **15**, 594 (2021).
- <sup>28</sup>A. Cvitkovic, N. Ocelic, and R. Hillenbrand, "Analytical model for quantitative prediction of material contrasts in scattering-type near-field optical microscopy," *Opt. Express* **15**, 8550–8565 (2007).